Sr₂Fe₁.₅Mo₀.₅O₆₋δ as a regenerative anode for solid oxide fuel cells

Qiang Liu[a], Daniel E. Bugaris[b], Guoliang Xiao[a], Maxwell Chmara[c], Shuguo Ma[c],
Hans-Conrad zur Loye[b], Michael D. Amiridis[c], Fanglin Chen[a],*

[a] Department of Mechanical Engineering, University of South Carolina, Columbia, SC 29208, USA
[b] Department of Chemistry & Biochemistry, University of South Carolina, Columbia, SC 29208, USA
[c] Department of Chemical Engineering, University of South Carolina, Columbia, SC 29208, USA

ABSTRACT

Sr₂Fe₁.₅Mo₀.₅O₆₋δ (SFM) was prepared using a microwave-assisted combustion synthesis method. Rietveld refinement of powder X-ray diffraction data reveals that SFM crystallizes in the simple cubic perovskite structure with iron and molybdenum disordered on the B-site. No structure transition was observed by variable temperature powder X-ray diffraction measurements in the temperature range of 25–800 °C. XPS results show that the iron and molybdenum valences change with an increase in temperature, where the mixed oxidation states of both iron and molybdenum are believed to be responsible for the increase in the electrical conductivity with increasing temperature. SFM exhibits excellent redox stability and has been used as both anode and cathode for solid oxide fuel cells. Presence of sulfur species in the fuel or direct utilization of hydrocarbon fuel can result in loss of activity, however, as shown in this paper, the anode performance can be regenerated from sulfur poisoning or coking by treating the anode in an oxidizing atmosphere. Thus, SFM can be used as a regenerating anode for direct oxidation of sulfur-containing hydrocarbon fuels.

1. Introduction

Solid oxide fuel cells (SOFCs) can efficiently convert the chemical energy of the fuel directly into electricity with fuel flexibility [1,2]. The current focus of SOFCs is primarily on systems consisting of an yttria-stabilized zirconia (YSZ) electrolyte and a porous Ni-YSZ cermet anode, which works well with H₂ and CO-based fuels. However, during direct oxidation of sulfur-containing hydrocarbon fuels, such as natural gas, the Ni-YSZ anode can be easily fouled by carbon deposition and sulfur poisoning [3]. Consequently, development of a cost effective anode material that can mitigate coking or sulfur poisoning is of great interest, as it will improve the performance and durability of SOFCs and enable them to operate by direct utilization of hydrocarbon fuels. By eliminating the need for external fuel reforming and sulfur removal components, the SOFC system can be greatly simplified and operate with much higher overall efficiency [4,5].

Recently, a new SOFC configuration using the same ceramic material for both electrodes, a so-called symmetrical SOFC, has been proposed and investigated [6,7]. The application of this fuel cell concept allows the anode to switch and become the cathode and *vice versa*, consequently providing a simple means to remove the coking problem by exposing the deactivated anode to an oxidizing atmosphere. Additionally, in the case of sulfur poisoning caused by reversible sulfur-adsorption at the anode, this new fuel cell configuration can potentially lead to a higher tolerance to sulfur-containing fuels. Furthermore, symmetrical SOFCs will reduce the number of fuel cell components from at least three materials to just two, consequently simplifying the fuel cell fabrication process and reducing the thermal stresses generated at the interfaces of different cell components. This can potentially lead to a significant reduction in the cost and an enhancement in the reliability of the SOFC system.

Much of the current interest in perovskites as electrode materials can be attributed to the work of Goodenough et al. on the Sr₂MgMoO₆₋δ system [5,8]. In order to improve the electrical properties of this system, the Mg²⁺ ions were replaced with Fe, which is capable of achieving oxidation states of +2 or +3 in this system. The redox couple Fe²⁺ + Mo⁶⁺ ↔ Fe³⁺ + Mo⁵⁺ is expected to generate electronic carriers, as well as to introduce oxygen vacancies into the lattice to allow ionic conduction [9,10]. By investigation of the Sr₂FeₓMo₂₋ₓO₆₋δ phase space, the Sr₂Fe₁.₅Mo₀.₅O₆₋δ (SFM) perovskite has been determined to be a promising electrode material for symmetrical SOFCs [11]. The conductivity of SFM in air and wet hydrogen can reach 21 and 13 S cm⁻¹ at 800 °C, respectively. In this paper, we have evaluated the structure, valence states, conductivity change, and regeneration properties of this material, with the ultimate goal of assessing the feasibility of using this material as a sulfur-tolerant anode for direct utilization of hydrocarbon fuels in SOFCs.

* Corresponding author. Tel.: +1 803 777 4875; fax: +1 803 777 0106.
E-mail address: chenfa@cec.sc.edu (F. Chen).

2. Experimental

2.1. Materials characterization

SFM was synthesized by a microwave-assisted combustion method. Details of the powder synthesis and cell fabrication can be found in our previous report [9]. Room-temperature X-ray diffraction measurement was done on a Rigaku Ultima IV diffractometer using Cu Kα radiation. Data were collected at a 0.02° step with a scan speed of 0.1° min^{-1} over the 2θ range 15–140°. Rietveld refinement of the data was performed using the GSAS software package and the EXPGUI interface [12,13]. A pseudo-Voigt function was used to model the peak profile and the background was described by a linear interpolation function. *In situ* high-temperature X-ray diffraction study was performed using a hot-stage-equipped Rigaku D/Max 2100 diffractometer using Cu Kα radiation. Data were collected at a 0.02° step for 2.4 s step^{-1} over the 2θ range 15–100°. The cell parameter at each temperature interval was obtained using the cell refinement function in JADE [14].

The microstructure and morphology of the samples were characterized by scanning electron microscopy (SEM, FEI Quanta 200) coupled with energy dispersive spectroscopy (EDS). X-ray photoelectron spectroscopy (XPS) data were collected with a Kratos Axis Ultra DLD instrument in both oxidizing and reducing atmospheres, at room temperature and at 550 °C.

Oxygen temperature-programmed desorption (O$_2$-TPD) was conducted on a ChemBET 3000 system. Prior to each O$_2$-TPD test, 100 mg of sample was degassed in nitrogen at 500 °C for 2 h. It was then treated in pure oxygen for 30 min before being cooled down to room temperature. The sample was then exposed to flowing helium and the temperature was ramped up at a rate of 20 °C min^{-1}, with the release of oxygen monitored through an on-line thermal conductivity detector (TCD).

2.2. Fuel cell testing

La$_{0.9}$Sr$_{0.1}$Ga$_{0.8}$Mg$_{0.2}$O$_3$ (LSGM) electrolyte supported symmetrical single cells with the configuration of SFM|LSGM|SFM were evaluated. LSGM electrolyte pellets (13 mm in diameter) were formed by uniaxially pressing LSGM powders under 200 MPa and then were sintered at 1400 °C in air for 5 h at a ramping rate of 2 °C min^{-1}. The resulting LSGM pellets had a thickness of around 0.4 mm. A slurry consisting of SFM and a Heraeus binder V006 (weight ratio of 1:1) was then applied to both surfaces of the electrolyte by screen-printing, and then fired at 1100 °C in air for 3 h to form porous electrode. The resulting electrode had a thickness of 40 μm and an effective electrode area of 0.33 cm^2. Gold paste was brushed on the anode side as current collector while Pt paste was applied on the cathode side as current collector.

The single cell was sealed on an alumina tube with a glass-ceramic sealant. The cathode side was open to air while the anode side was exposed to fuel at a flow rate of 40 mL min^{-1}. Electrochemical characterizations of the cells were performed under ambient pressure using a Versa STAT 3-400 test system (Princeton Applied Research). AC impedance spectroscopy was measured under open circuit conditions in the frequency range from 100 kHz to 0.01 Hz.

3. Results and discussion

3.1. XRD and TEM study

The phase space of Sr$_2$Fe$_x$Mo$_{2-x}$O$_6$ (0.8 ≤ x ≤ 1.5) has been structurally characterized by Rao and coworkers using powder X-ray diffraction [15]. For x ≤ 1.2, the structure has been assigned to a double perovskite in the space group I4/mmm of the tetragonal system.

Table 1

Structural parameters and selected interatomic distances for Sr$_2$Fe$_{1.5}$Mo$_{0.5}$O$_{6-\delta}$ obtained from Rietveld refinement of powder X-ray diffraction data. Atomic positions are Sr (0.5, 0.5, 0.5), Fe/Mo (0, 0, 0), and O (0, 0, 0.5) in space group Pm-3m of the cubic system.

Temperature (K)	298
a (Å)	3.92874(6)
Volume (Å^3)	60.640(3)
R_p (%)	5.80
R_{wp} (%)	8.29
χ^2	3.026
Sr (B_{iso}) (Å^2)	1.03(2)
Fe/Mo (B_{iso}) (Å^2)	0.58(3)
O (B_{iso}) (Å^2)	1.79(6)
Sr–O × 12 (Å)	2.78804(3)
Fe/Mo–O × 6 (Å)	1.96437(3)

For x > 1.2, the structure has been solved as a double perovskite in space group Fm-3m of the cubic system. The ordering of Fe and Mo on the B and B′ sites has a maximum at x = 0.95, and decreases as x deviates from this value. For the compound Sr$_2$Fe$_{1.5}$Mo$_{0.5}$O$_6$, the Fe occupancy of the B (0, 0, 0) and B′ (0, 0, 0.5) sites is 0.7402(127) and 0.7598(127), respectively. Within error, this is the 3:1 iron-to-molybdenum ratio expected from the nominal stoichiometry of the phase. The Fe and Mo cations are fully disordered on both the B and B′ sites of the cubic double perovskite structure. Therefore, we have instead solved the structure of Sr$_2$Fe$_{1.5}$Mo$_{0.5}$O$_{6-\delta}$ as a fully disordered simple cubic perovskite. (We note here that Rao et al. most likely refined the structure of Sr$_2$Fe$_{1.5}$Mo$_{0.5}$O$_6$ in space group Fm-3m for ease of comparison with the phases where x = 1.3 and x = 1.4.)

Rietveld refinement of the powder X-ray diffraction data for Sr$_2$Fe$_{1.5}$Mo$_{0.5}$O$_{6-\delta}$ converges to a satisfactory solution in space group Pm-3m of the cubic system (Table 1). The experimental and calculated patterns and the difference between them, as well as the expected Bragg peak positions for Sr$_2$Fe$_{1.5}$Mo$_{0.5}$O$_{6-\delta}$ are displayed in Fig. 1. If the lattice parameter from Sr$_2$Fe$_{1.5}$Mo$_{0.5}$O$_{6-\delta}$ in the cubic simple perovskite structure (a_p) is transformed into that of the cubic double perovskite structure ($2a_p$), a value of 7.85748(6) Å is obtained. This value is slightly smaller than the lattice parameter of 7.8717(1) Å for Sr$_2$Fe$_{1.5}$Mo$_{0.5}$O$_6$ reported by Rao. The reason for this is the difference in ionic radii [16] between six-coordinate Fe^{2+} (0.78 Å) and six-coordinate Fe^{3+} (0.645 Å), as well as those
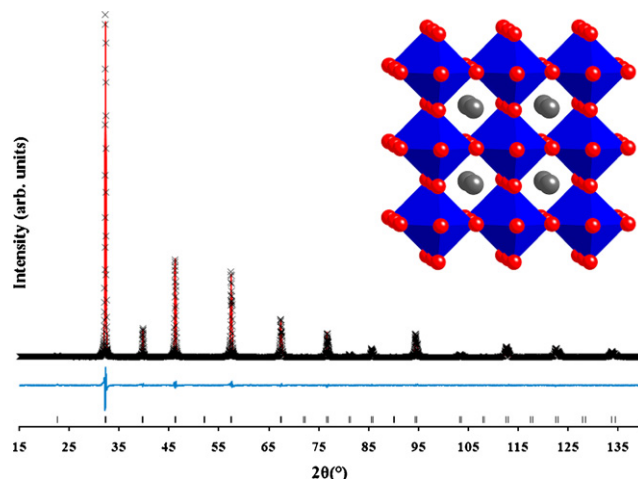
Fig. 1. Rietveld refinement of powder X-ray diffraction data for Sr$_2$Fe$_{1.5}$Mo$_{0.5}$O$_{6-\delta}$. Crosses are observed data, the solid red line is the calculated pattern, and the blue line is the difference. Tick marks indicate the allowed Bragg reflections. The inset is the crystal structure of Sr$_2$Fe$_{1.5}$Mo$_{0.5}$O$_{6-\delta}$. Blue octahedra represent disordered Fe (75%) and Mo (25%) atoms, gray spheres represent Sr atoms, and red spheres represent O atoms.
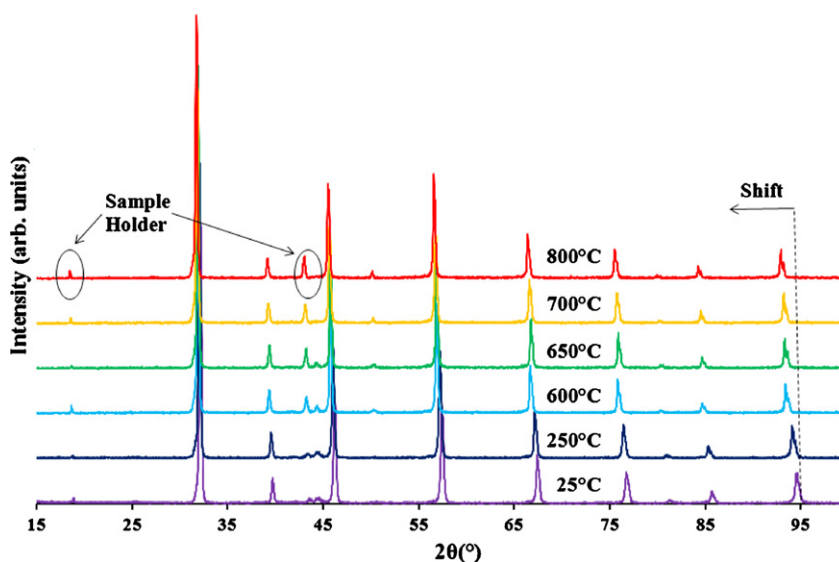
Fig. 2. *In situ* high-temperature powder X-ray diffraction data for $Sr_2Fe_{1.5}Mo_{0.5}O_{6-\delta}$ over the temperature range 25–800 °C.

of six-coordinate Mo^{5+} (0.61 Å) and six-coordinate Mo^{6+} (0.59 Å) [16]. The $Sr_2Fe_{1.5}Mo_{0.5}O_6$ sample had been subjected to sintering at 1280 °C for 12 h in a stream of 5% H_2/Ar in Rao's study, which is expected to reduce the sample, thereby increasing the proportion of the larger Fe^{2+} and Mo^{5+} cations. However, prior to X-ray diffraction, the $Sr_2Fe_{1.5}Mo_{0.5}O_{6-\delta}$ sample had only undergone microwave-combustion and calcination in air at 1000 °C in this study, and therefore should contain primarily the smaller Fe^{3+} and Mo^{6+} cations, as evidenced by XPS (see discussion below).

No structural transition for $Sr_2Fe_{1.5}Mo_{0.5}O_{6-\delta}$ is observed in the *in situ* high-temperature powder X-ray diffraction in the temperature range of 25–800 °C (Fig. 2). Furthermore, no additional phases appear over the given temperature range, suggesting that the compound is stable in air up to 800 °C. The peaks in the diffraction pattern shift to lower 2θ angles as the temperature increases, resulting in an increase in lattice parameter with temperature (Fig. 3). From the high-temperature powder X-ray diffraction data, the isotropic thermal expansion coefficient is determined to be $6.9(2) \times 10^{-5}$ Å °C^{-1}.

TEM studies were undertaken to evaluate the local crystal structure. Several selected area electron diffraction (SAED) patterns along the [1 1 1] and [1 1 0] zone axes and on different grains were

taken as shown in Fig. 4. They can be indexed to the cubic simple perovskite structure with a lattice parameter of $a \sim 3.9$ Å where the reflection conditions correspond to space group Pm-$3m$ [17] consistent with the absence of B-site cation ordering as determined by the Rietveld analysis of powder X-ray diffraction data.

Interestingly, relatively high intensity streaks along [1 1 1] in the (1 1 0) diffraction pattern were observed for some grains, which could be interpreted as either local B-site cation ordering [17], the overlap of stacking fault-derived scattering [17], or as an ordering of oxygen vacancies [18]. Recently, Meneghini et al. have reported the results of their simulation study of Sr_2FeMoO_6, suggesting that a very high degree of short range ordering is preserved even in samples that appear to be fully disordered macroscopically. Thus, it is possible that anti-site defects are not homogeneously distributed throughout the sample and that nano-sized anti-phase domains are present in the system [19]. However, our SFM system has a very different iron to molybdenum ratio (1.5:0.5) than that of Sr_2FeMoO_6 (1:1), which in fact requires anti-site disorder. Generally, in double perovskites, B-site ordering results from the size and charge differences of the two cations. Hence it is possible that due to the presence of Fe^{2+}/Fe^{3+} and Mo^{5+}/Mo^{6+} couples in $Sr_2Fe_{1.5}Mo_{0.5}O_{6-\delta}$, some local ordering exists on the nanoscale.

3.2. XPS analysis

Our experimental data show that relative to the electronic conductivity, the ionic conductivity is negligible [10]. Consequently, the measured total conductivity represents primarily the electronic conductivity. For perovskite oxides, the electronic conductivity is closely related to the crystal structure and the presence of mixed valency on the B-site [20]. As no structure transition was detected in the high-temperature powder X-ray diffraction data (Fig. 2), it is likely that the increase in the total electrical conductivity with temperature may be related to the change in the degree of mixed valency caused by oxygen loss with the increase in temperature.

Investigations of the B-site mixed valency can provide additional insight into the reasons for the observed high electrical conductivity in SFM. XPS measurements were carried out to study the iron and molybdenum oxidation states in SFM as a function of temperature (Fig. 5). The XPS analysis was performed on the Fe $2p_{3/2}$ excitations (Fig. 5a). Data analysis of the Fe $2p_{3/2}$ level confirms that iron in SFM exists as both Fe^{3+} (binding energy = 710.4 eV)
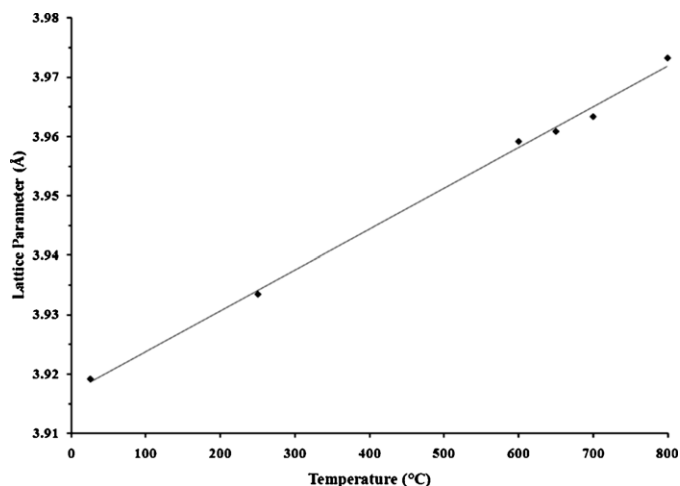
Fig. 3. Plot of lattice parameter (Å) versus temperature (°C) for $Sr_2Fe_{1.5}Mo_{0.5}O_{6-\delta}$, along with a straight line fit showing the isotropic thermal expansion.
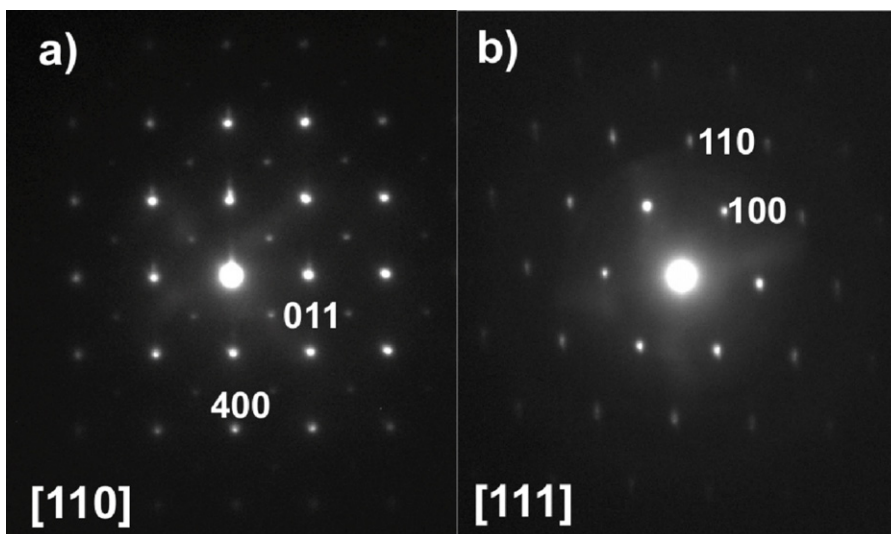
Fig. 4. SAED patterns of (a) [1 1 0], and (b) [1 1 1] zone axes for $Sr_2Fe_{1.5}Mo_{0.5}O_{6-\delta}$.

and Fe^{2+} (709.2 eV), in good agreement with results reported by Zhang et al. [21]. Fig. 5b shows the Mo 3d core-level spectra of the SFM sample at room temperature. A curve-fitting analysis of the Mo $3d_{5/2}$ spectra yields two contributions to the data, one from Mo^{6+} at 232.1 eV, and one from Mo^{5+} at 231.6 eV. It can be clearly seen that the valences of Fe and Mo change significantly as a consequence of the heat treatments, which should correlate with the samples' oxygen content. At room temperature, the majority of the iron and molybdenum cations exist as Fe^{3+} and Mo^{6+}, shifting to 32.4% Fe^{2+} and 61.1% Mo^{5+} at 550 °C, the upper temperature limit for the XPS instrument available to this study. It can be clearly seen that the Fe^{2+} and Mo^{5+} content increase with the increase in temperature, where the relative ratio of Fe^{2+}/Fe^{3+} and Mo^{5+}/Mo^{6+} will influence the electronic conductivity via the $Fe^{3+} + Mo^{5+} \leftrightarrow Mo^{6+} + Fe^{2+}$ process [22]. Consequently, the oxide ion conductivity should increase due to an increase in the number of oxygen vacancies. There may be an upper limit to the oxygen vacancies in SFM. According to Goodenough et al., the Mo^{6+}/Mo^{5+} redox band can overlap with the Fe^{3+}/Fe^{2+} couple and protect iron from being fully reduced to the metallic state [23]. In any case, regardless of the limit of the total oxygen deficiency in this oxide, it does not reach the point where the structure collapses. This behavior is further supported

by the results of our oxygen temperature-programmed desorption (O_2-TPD) experiments.

3.3. TPD characterization

A typical O_2-TPD profile of SFM is shown in Fig. 6, where the oxygen evolution is measured as a function of the operating temperature. For comparison, the corresponding O_2-TPD profile of Sr_2MgMoO_6 (SMM) is also provided in Fig. 6, indicating significant differences between the two materials. Two types of desorbed oxygen, corresponding to the two peaks in the O_2-TPD profiles, have been widely reported in the literature for perovskite-type materials, with significantly different temperatures of desorption [24,25]. The first type is designated as α-O_2 and is associated with surface oxygen species desorbing at temperatures below 700 °C. The second type is denoted as β-O_2 and has been attributed to either lattice or interstitial oxygen species desorbing at temperatures above 800 °C. As shown in Fig. 6, surface oxygen desorbs from SFM, while lattice or interstitial oxygen desorbs from SMM. This result suggests that oxygen vacancies form more readily on the surface of SFM at intermediate temperatures than on the surface of SMM. In contrast, SMM loses significant quantities of lattice oxygen at tem-
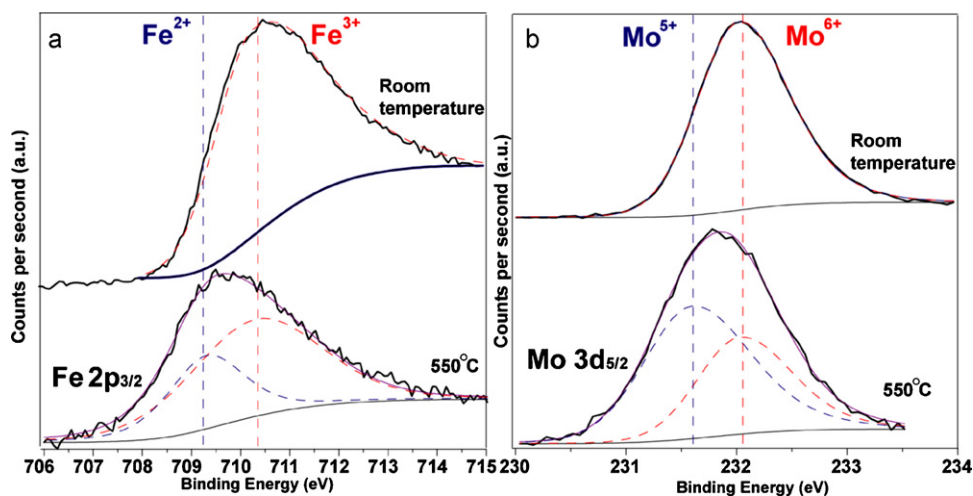
Fig. 5. XPS spectra and curve-fitting of (a) Fe 2p and (b) Mo 3d core-level of $Sr_2Fe_{1.5}Mo_{0.5}O_{6-\delta}$ at room temperature and 550 °C.
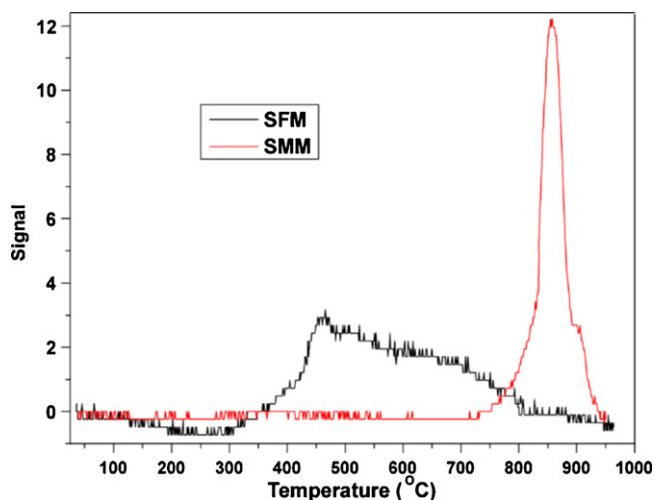
Fig. 6. TPD profiles of Sr_2MgMoO_6 (SMM) and $Sr_2Fe_{1.5}Mo_{0.5}O_{6-\delta}$ (SFM).

Fig. 7. Stability of the SFM|LSGM|SFM single cell at 800 °C versus the time of stream after 10 cycles. In the first 5 cycles are redox cycle test, the anode gas was switched between air and H_2; In the last 5 cycle tests, the anode gas was switched between H_2 and H_2 with 100 ppm H_2S. The maximum power density was recorded after each cycle.

peratures above 800 °C, as indicated by the large peak centered at 850 °C, which is not observed for SFM, where oxygen evolution is minimal within that temperature ranges. Apparently, the presence of iron ions in SFM allows for significant reduction (Fe^{3+} to Fe^{2+} and perhaps Mo^{6+} to Mo^{5+}) at a lower temperature, a process that is completed by 900–1000 °C. In contrast, the magnesium ions in SMM are not reducible, and therefore, the high temperature oxygen evolution should be attributed exclusively to the reduction of Mo^{6+} to Mo^{5+}. In both cases, oxygen vacancies are present at high temperatures.

The results of the XPS and TPD studies suggest the presence of significant oxygen vacancies in SFM, which are expected to lead to substantial oxide ion conductivity. In fact, the oxide ion conductivity of SFM has been measured to reach 0.13 S cm^{-1} at 800 °C in air, which is significantly higher than that of the current state-of-the-art cathode material for SOFCs, $La_{0.8}Sr_{0.2}MnO_3$, which has an oxide ion conductivity of only 5.93×10^{-7} S cm^{-1} at 800 °C, and comparable to that of the Co-based cathode material, $La_{0.6}Sr_{0.4}CoO_3$, which has an oxide ion conductivity of 0.22 S cm^{-1} at 800 °C [10].

3.4. Cell regenerative test

SFM was used as both the anode and the cathode material in the symmetrical SOFC with the configuration of SFM|LSGM|SFM, and was operated at a constant cell voltage of 0.5 V to determine the cell performance and the overall performance stability. As shown in Fig. 7, after undergoing five redox cycling tests at 800 °C, the maximum power output of the symmetrical SOFC remains stable, suggesting that SFM has very good redox stability.

The good redox stability prompted us to further evaluate SFM as a regenerating anode to mitigate sulfur poisoning and coking issues that are typically encountered during the direct oxidation of sulfur-containing hydrocarbon fuels. Sulfur tolerance and the recovery of the catalytic activity of the anode from sulfur poisoning are major concerns for the durability and reliability of the fuel cells. Regenerating characteristics of the SFM anode were evaluated by cyclic testing of the fuel cell operated between H_2 and H_2 with 100 ppm H_2S. As shown in Fig. 7, after operating in H_2 with 100 ppm H_2S for 6 h at 800 °C, a 10% current drop was observed, which is much better than that of a typical Ni-based cermet anode operated under similar conditions. To evaluate if the anode could be regenerated, the sulfur-poisoned anode was heated in air at 800 °C for 3 h. As shown in Fig. 7, the cell performance was almost fully recovered following such a regeneration treatment. The sulfur-poisoning and oxidation regeneration process was repeated 5 times, and no obvious signs of
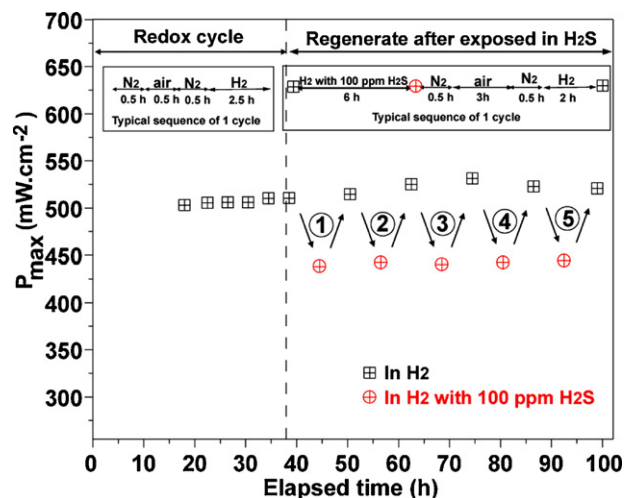
permanent anode deactivation were observed, demonstrating that SFM can be applied as a sulfur-tolerant anode in SOFCs.

Finally, since SOFCs have the ability to directly utilize hydrocarbon fuels without external reforming, the regeneration of the fuel cell from anode coking deactivation is also important. It should be noted that in the symmetrical SOFC using SFM as the electrode, the cell performance is much higher using H_2 as the fuel compared with that using CH_4 as the fuel. For example, the peak cell power density at 850 and 900 °C using CH_4 as the fuel are only 125 and 250 mW cm^{-2}, respectively [9]. Previous studies show that the ideal anode for direct oxidation of hydrocarbons satisfies the following merits [26]: high electrocatalytic activity for the reaction of the hydrocarbon with oxide ions at the three phase boundary (TPB) and high catalytic activity for the reaction of the hydrocarbon with the produced H_2O (steam reforming), or hydrocarbon directly cracking, which can be expressed by the following three reactions:

$$CH_4 + 4O^{2-} \rightarrow 2H_2O + CO_2 + 8e^- \tag{1}$$

$$CH_4 + H_2O \rightarrow CO + 3H_2 \tag{2}$$

$$CH_4 \rightarrow C + 2H_2 \tag{3}$$
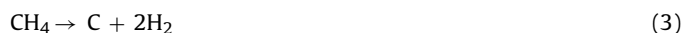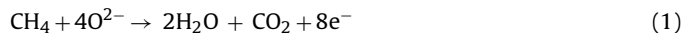
It seems that the first mechanism is unlikely to be associated with the SFM anode; otherwise there should not display such obvious cell performance drop when the fuel was switched from H_2 to CH_4. Therefore, the sluggish performance in CH_4 can be attributed to the relatively low catalytic activity of SFM for CH_4 reforming/cracking, a phenomena that has also been observed in other oxide based ceramic anode. Bossche et al. found that the dominant reaction mechanism in the $La_{0.75}Sr_{0.25}Cr_{0.50}Mn_{0.50}O_{3-\delta}$ oxide anode is reaction 3 [27]. Considering the following regenerative experimental results, coking had indeed occurred when operating the cell using CH_4 as fuel. Consequently, it is believed that the third reaction is also the main mechanism for the SFM anode. Therefore, one of the efficient ways to improve the SFM anode performance for direct hydrocarbon operations is to introduce transition metals (Ni, Ru, Ir, etc.), which show excellent catalytic activity for hydrocarbon reforming, to the SFM anode [26]. Our recent work indicates that with even 2 wt% Ni infiltrated to the SFM anode; the cell performance using CH_4 as the fuel can be dramatically improved [28].

As discussed above, when using CH_4 as the fuel, the operating temperature has a significant effect on the anode coking problem, with higher cell operating temperatures leading to faster deac-
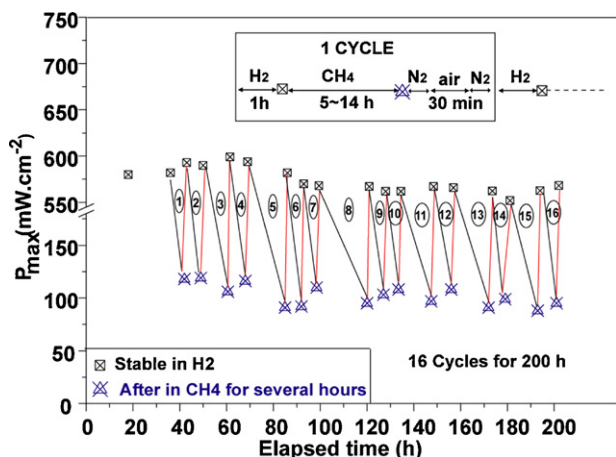
Fig. 8. Stability of the SFM|LSGM|SFM single cell at 850 °C versus the time of stream after 16 cycles, in which the anode gas was switched between H_2, air and CH_4. The maximum power density was recorded after each cycle.

tivation [29]. To illustrate the regenerating efficiency, a higher operating temperature (850 °C) was chosen to accelerate anode deactivation due to coking. Prior to conducting the anode regenerative test in CH_4, the fuel cell was operated using H_2 (with 3 vol% H_2O) as the fuel for 15 h at 850 °C, and the stability of the cell performance was confirmed under these operating conditions. The sequence of one anode coking and regeneration cycle is illustrated in the inset in Fig. 8, where after operating the cell using H_2 as the fuel for 1 h, the anode was exposed to CH_4 (with 3 vol% H_2O). The cell using CH_4 as the fuel typically exhibited a gradual decrease in cell performance. For regeneration, air was introduced to the anode for 30 min to remove any coke formed. The anode compartment was briefly purged with N_2 between switching the gas stream from CH_4 to air or from air to CH_4. As shown in Fig. 8, after operating the cell using H_2 as the fuel for 40 h, the anode regenerating test was started and the maximum power output of the cell did not change significantly after 16 regeneration cycling tests that lasted for 200 h, indicating that SFM can be potentially used as a regenerating anode material in fuel cells for direct utilization of hydrocarbon fuels.

4. Conclusion

SFM has been found to possess a simple cubic perovskite structure with no phase change from room temperature to 800 °C in air. Electrical conductivity of SFM changes as a function of temperature due to the valence changes of iron and molybdenum ions in the structure. SFM has been shown to exhibit excellent redox stability and can be regenerated from sulfur poisoning and coking by exposing the deactivated anode to an oxidizing atmosphere at the cell operating temperature. This regenerating concept may point to a new direction for the development of durable SOFCs that can operate efficiently using sulfur-containing hydrocarbon fuels.

References

[1] A.J. Jacobson, Chem. Mater. 22 (2010) 660.
[2] B. Zhu, Int. J. Energy Res. 33 (2009) 1126.
[3] N.P. Brandon, S. Skinner, B.C.H. Steele, Annu. Rev. Mater. Res. 33 (2003) 183.
[4] A. Atkinson, S. Barnett, R.J. Gorte, J.T.S. Irvine, A.J. McEvoy, M. Mogensen, S.C. Singhal, J. Vohs, Nat. Mater. 3 (2004) 17.
[5] Y.H. Huang, R.I. Dass, Z.L. Xing, J.B. Goodenough, Science 312 (2006) 254.
[6] J. Canales-Vazquez, J.C. Ruiz-Morales, D. Marrero-Lopez, J. Pena-Martinez, P. Nunez, P. Gomez-Romero, J. Power Sources 171 (2007) 552.
[7] J.C. Ruiz-Morales, J. Canales-Vazquez, B. Ballesteros-Perez, J. Pena-Martinez, D. Marrero-Lopez, J.T.S. Irvine, P. Nunaz, J. Eur. Ceram. Soc. 27 (2007) 4223.
[8] Y.H. Huang, R.I. Dass, J.C. Denyszyn, J.B. Goodenough, J. Electrochem. Soc. 153 (2006) A1266.
[9] Q. Liu, X.H. Dong, G.L. Xiao, F. Zhao, F.L. Chen, Adv. Mater. 22 (2011) 5478.
[10] G.L. Xiao, Q. Liu, F. Zhao, L. Zhang, C. Xia, F.L. Chen, J. Electrochem. Soc. 158 (2011) B455.
[11] Q. Liu, G.L. Xiao, T. Howell, T. Reitz, F.L. Chen, ECS Trans. 35 (2011) 1357.
[12] B.H. Toby, J. Appl. Crystallogr. 34 (2001) 210.
[13] A.C. Larson, R.B. von Dreele, General Structure Analysis System (GSAS) , Los Alamos National Laboratory, 1990.
[14] JADE Version 9.0, Materials Data Inc., 2010.
[15] G.Y. Liu, G.H. Rao, X.M. Feng, H.F. Yang, Z.W. Ouyang, W.F. Liu, J.K. Liang, J. Alloys Compd. 353 (2003) 42.
[16] R.D. Shannon, Acta Crystallogr. Sect. A 32 (1976) 751.
[17] Z.Q. Deng, J.P. Smit, H.J. Niu, G. Evans, M.R. Li, Z.L. Xu, J.B. Claridge, M.J. Rosseinsky, Chem. Mater. 21 (2009) 5154.
[18] E. Bucher, W. Sitte, I. Rom, I. Papst, W. Grogger, F. Hofer, Solid State Ionics 152 (2002) 417.
[19] C. Meneghini, S. Ray, F. Liscio, F. Bardelli, S. Mobilio, D.D. Sarma, Phys. Rev. Lett. 103 (2009) 046403.
[20] H.X. Gu, Y. Zheng, R. Ran, Z.P. Shao, W.Q. Jin, N.P. Xu, J. Ahn, J. Power Sources 183 (2008) 471.
[21] L.L. Zhang, Q.J. Zhou, Q.A. He, T.M. He, J. Power Sources 195 (2010) 6356.
[22] M.S. Moreno, J.E. Gayone, M. Abbate, A. Caneiro, D. Niebieskikwiat, R.D. Sanchez, A. de Siervo, R. Landers, G. Zampieri, Solid State Commun. 120 (2001) 161.
[23] J.B. Goodenough, Y.H. Huang, J. Power Sources 173 (2007) 1.
[24] B. Levasseur, S. Kaliaguine, Appl. Catal. B 88 (2009) 305.
[25] J. Liu, Z. Zhao, J. Lan, C.M. Xu, A.J. Duan, G.Y. Jiang, X.P. Wang, H. He, J. Phys. Chem. C 113 (2009) 17114.
[26] T. Hibino, A. Hashimoto, M. Yano, M. Suzuki, M. Sano, Electrochim. Acta 48 (2003) 2531.
[27] M.K. Bruce, M. van den Bossche, S. McIntosh, J. Electrochem. Soc. 155 (2008) B1202.
[28] G.L. Xiao, F.L. Chen, Electrochem. Commun. 13 (2011) 57.
[29] S. McIntosh, R.J. Gorte, Chem. Rev. 104 (2004) 4845.